Shap. Mem. Superelasticity (2020) 6:287–300
https://doi.org/10.1007/s40830-020-00299-7

SPECIAL ISSUE: A TRIBUTE TO PROF. DR. GUNTHER EGGELER, INVITED PAPER

Recent Developments in Small-Scale Shape Memory Oxides

Xiao Wang[1] · **Alfred Ludwig**[1]

Published online: 26 August 2020

Abstract This review presents an overview of the developments in small-scale shape memory materials: from alloys to oxides and ceramics. Shape memory oxides such as zirconia, different ferroelectric perovskites and VO_2-based materials have favorable characteristics of high strength, high operating temperature and chemical resistance, which make this class of shape memory materials interesting for special applications, e.g., in harsh environments or at the nanoscale. Because of the constraint and mismatch stress from neighboring grains in polycrystalline/bulk oxides, the transformation strain of shape memory oxides is relatively small, and micro-cracks can appear after some cycles. However, recent progress in shape memory oxide research related to small-scale approaches such as decreasing the amounts of grain boundaries, strain-engineering, and application in the form of nanoscale thin films shows that some oxides are capable to exhibit excellent shape memory effects and superelasticity at nano/micro-scales. The materials systems ZrO_2, $BiFO_3$, and VO_2 are discussed with respect to their shape memory performance in bulk and small-scale.

Keywords Shape memory ceramics · Shape memory films · Mechanical behavior

Introduction

Shape memory alloys (SMAs) undergo a reversible, diffusionless, solid-state phase transformation between martensitic and austenitic crystal structures in response to external stimuli (temperature, stress, electric field, magnetic field, or combinations thereof), accompanied by strains ranging up to and beyond 10%. The ability of returning to its original shape upon heating was defined as shape memory effect (SME) [1, 2]. At least two crystal structures are involved, i.e., austenite and martensite. Austenite is stable at high temperature ($T > A_F$, austenite finish temperature) and transforms to twinned martensite upon cooling ($T < M_S$, martensite start temperature). Upon loading, twinned martensite converts to detwinned martensite, with strain generated and remaining after unloading. Detwinned martensite transforms to austenite by heating, with the shape recovered. This cycle is called one-way SME. The shape can also be remembered in both states, when the material shows the two-way SME or reversible SME. In addition, a reversible transformation between austenite and martensite at $T > A_F$, by applying mechanical load is called superelasticity (SE).

During the past decades, SMAs have been extensively investigated in terms of fundamental mechanism and engineering applications, for instance the most commercial SMAs, NiTi alloys, show excellent SME and mechanical properties [3, 4]. SMAs have been used in numerous fields, such as microelectromechanical systems (MEMS) [5, 6], medicine [7, 8], automotive [9], and aerospace [10]. However, conventional SMAs can suffer from oxidation

This invited article is part of a special issue of *Shape Memory and Superelasticity* to honor Prof. Dr.-Ing. Gunther Eggeler. This special issue was organized by Prof. Hüseyin Sehitoglu, University of Illinois at Urbana-Champaign, and Prof. Dr.-Ing. Hans Jürgen Maier, Leibniz Universität Hannover.

✉ Alfred Ludwig
alfred.ludwig@rub.de

[1] Chair for Materials Discovery and Interfaces, Institute for Materials, Ruhr University Bochum, 44801 Bochum, Germany

and instability, especially in nanoscale [11, 12], e.g., Ti content in NiTi unavoidably leads to changes in surface and interfacial layers due to oxidation, thereby reducing transforming performance [13].

SMEs are also observed in some oxides, so-called shape memory oxides (SMOs). Two types are mainly of interest in research: martensitic shape memory ceramics and ferroelectric shape memory ceramics [2]. Compared to SMAs, SMOs have high strength, high-temperature operation and chemical resistance, which could fulfill some application needs that SMAs can't [1, 14, 15]. Details on the fundamental mechanism of different types of SMOs can be found in review articles [2, 14, 16], which therefore will not be focused in this review. The drawbacks of SMOs are that the magnitude of recoverable strain is relatively low and micro-cracking can appear during transformation cycling. For example, cracking was observed in polycrystalline ZrO_2 (zirconia) after about 5 cycles transformation cycles, in which about $\sim$ 2% of strain was achieved [17]. The transformation mismatch stress developed during the phase transformation, especially between neighboring grains of different orientations, leads to the formation of micro-cracks and fracture most often along grain boundaries. Latest studies on the small-scaling of SMOs pave a way for overcoming issues with brittleness and thus facilitating practical applications of SMOs. Some SMOs at the micro/nanoscales are capable to exhibit profound SE and SME [18, 19].

This review mainly summarizes the recent progress in the research of the mechanical performance of SMOs at small scales. First, the concept and application of small-scaling in SMA is presented. Second, three SMO material systems, based on zirconia (ZrO_2), bismuth ferrite ($BiFeO_3$), and vanadium dioxide (VO_2), on which micro/-nanoscale methodology have been proven to be effective, are presented.

Concepts and Characteristics of SMAs and SMOs at Small Scales

The exploration of small-scaling effects on SME/SE started on SMAs, e.g., for the application of these alloys in miniaturized functional devices such as MEMS. Studies on NiTi-based SMA, the most extensively researched SMA material system, show that the martensitic transformation of SMA and the accompanying SME and SE properties are strongly affected by the grain size at the nanoscale. In the case that the grain size d is much finer than the sample size D, the parent austenite phase is completely stabilized once d is smaller than a critical value, typically in the range of several tens of nanometers. The martensitic transformation is therefore suppressed [12]. For example, Waitz et al. [20] reported that the transformation of nanocrystalline NiTi SMAs to martensite is no longer observed once d reaches a critical size. In study of the size dependence of the martensitic transformation in SMAs, a model was proposed with respect to the transformation thermodynamics in nanocrystalline NiTi [20]. The following relations applies during the transformation: $\Delta G^{A-M} = E_b$, with $\Delta G^{A-M} = G^A - G^M$ being the chemical free energy difference per unit volume between the austenite G^A and martensite G^M, and $E_b = E_s + E_i + E_f$ being the energy barrier per unit of transformed volume which includes the increase in the total elastic strain energy E_s, interface energy E_i associated with the formation of martensite in austenite matrix and total irreversible frictional energy E_f of the transformation. By calculation, it was concluded that the E_b of the transformation to martensite increases with decreasing grain size. As a result, the martensitic phase transformation is suppressed when the grain size is < 100 nm and completely suppressed at a critical size of 50 nm.

In contrast, when d is comparable to D, nanoscale SMAs can show excellent properties. For example, Juan et al. [21] performed nanocompression test on pillars of various size made from single-crystal Cu–Al–Ni alloys, and found that both austenite and martensite are more stable in nanoscale pillars than they are in bulk. The stress–strain curve (Fig. 1b) during the martensitic transformation exhibits a large hysteresis area in the closed loading–unloading loop, which suggests a very high figure of merit for mechanical damping. This size effect makes Cu–Al–Ni nano/microstructures attractive for damping applications in nano- and microscale devices. Further, Cu–Al–Ni small-scale pillars show a strong size effect on the critical stress that induces the martensitic transformation, in which a power-law size dependence is observed for the nanoscale SE [22]. It is noteworthy that the concept of small-scale pillar is not applicable to NiTi SMA: similar compression test on sub-micropillars shows a loss of PE for samples with diameter < 200 nm, although in situ TEM observations confirm the occurrence of martensitic transformation [23, 24]. It was proposed that the loss of PE is related to a suppression of strain recovery, which might be due to a Ga^+ ion damage layer from FIB fabrication of the pillar [25].

Oligocrystalline shape memory alloys (oSMAs) [26–28] are investigated as they show a greater total surface area than total grain boundary area. Because of less transformation strain at grain boundaries and triple junctions, oSMAs can achieve single crystal-like SMAs properties without failure or fracture. For example, Cu–Al–Ni oSMAs wires show recoverable strain up to $\sim$ 7%. In comparison, bulk SMAs normally fracture at very small strain (Fig. 1c). oSMAs structures show increase in cycle life of up to two orders of magnitude over polycrystals. Size effects in both the transformation stresses and temperature of Cu–Al–Ni

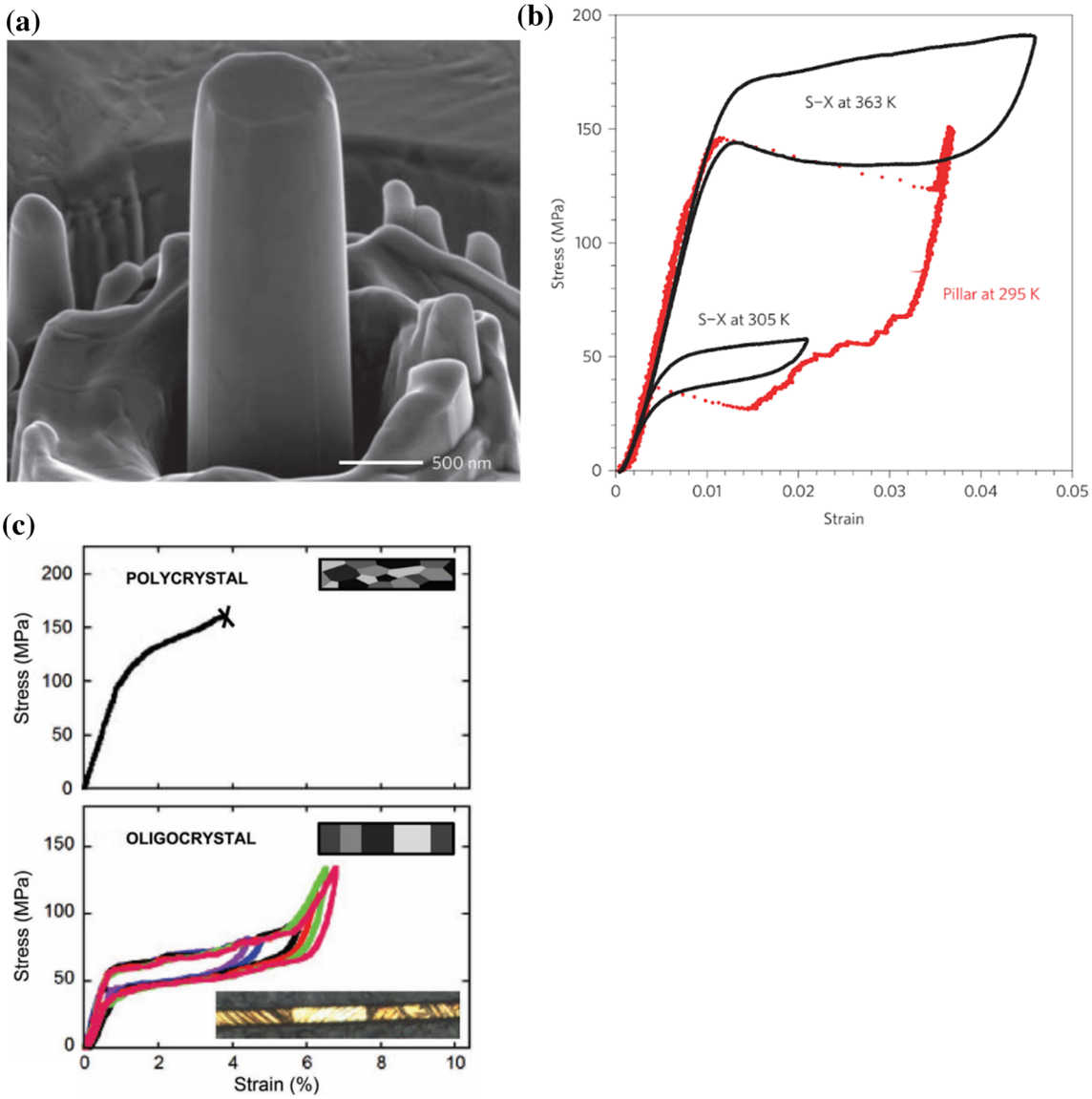

Fig. 1 **a** SEM image of a submicrometer pillar milled by FIB on a Cu–Al–Ni [001] oriented single crystal. **b** Comparison of the compression behavior in bulk single crystals Cu–Al–Ni (black curves) at 363 and 305 K, and submicrometer pillar at 295 K. "Reprinted from Reference [21] with permission, Copyright (2009), Springer Nature." **c** Stress–strain curves of polycrystalline Cu–14.1Al–4.2Ni and oligocrystalline Cu–13.7Al–5Ni. The schematics in the top right corner of each graph show the grain structure of each sample. "Reprinted from Reference [27] with permission, Copyright (2012), John Wiley and Sons"

oSMAs were observed, and an increase in the hysteresis area in the stress–strain loop in oSMAs with smaller size was also observed, which suggests the application for energy damping.

In summary two methods are used to improve the shape memory performance of SMAs. One method is to reduce the size of the sample, because a smaller sample leads to a higher surface-to-volume ratio and lattice dilation and mismatch stresses from the transformation can be relaxed at free surface. The other method is to reduce the number of grains in the sample, e.g., to use an oligocrystal or single crystal, which can reduce the stress mismatch and transformation constraint occurring at the grain boundary area. As mentioned above in the thermodynamic equation, energy barrier E_s is attributed to the elastic mismatch stresses induced by the phase transformation, when the dilatation of the transformed region is accommodated by the surrounding austenite matrix. When it comes to the micro-scale pillar or oSMAs, E_s is largely reduced because the mismatch stress can be relaxed at larger free surface region. Meanwhile, transformation constraint from the grain boundaries is also reduced. As a result, the microscale pillar and oSMAs can show excellent SMEs [21, 27].

SMEs of thin film SMA were also researched, showing interesting properties and giving more insights into its nanoscale application. For example, a study on B2–B19 martensitic transformation in $Ti_{51}Ni_{38}Cu_{11}$ thin film with thickness ranging from 750 to 50 nm shows that A_F and M_S temperatures decreased with decreasing film thickness but increased again for film thickness < 100 nm [29]. The 75 nm thick film showed zero hysteresis and an A_F well above room temperature, which make it promising for nanoscale application. Although it was mentioned that the transformation of NiTi is suppressed for very small grain sizes, substrate-attached $Ti_{51}Ni_{38}Cu_{11}$ thin films as thin as 50 nm still exhibit phase transformation. Studies on SMA thin films also suggest that the effect of the surface reaction layer should be considered when nanoscale shape memory thin films are used. For instance, the reaction layers formed on the surface of $Ti_{51}Ni_{38}Cu_{11}$ thin film significantly change the chemical composition of the transforming phase [13]. As a result, the phase transformation properties are influenced by film thickness, because the deviation from the nominal chemical composition is larger for thinner films. For example, for a 50 nm thin film, the Ti content was reduced by 9 at.%, whereas the Ni content was increased by 5 at.%. The Cu content stays relatively constant for films of different thickness. To investigate the scaling effects in SMA thin films, some micromachined test platforms such as microfabricated devices and thin film microbridges were designed [30]. Those devices allow for nanomechanical tests and enable electrical characterization before, during, and after the performance of these tests. Furthermore, in situ TEM nanomanipulation on free-standing thin film microbridges is possible with the device.

ZrO_2

Low Recoverable Strain of SME in Polycrystalline/Bulk ZrO_2

ZrO_2 has three polymorphs: monoclinic (m), tetragonal (t) and cubic (c), among which, the t-m martensitic transformation is of interest because of the accompanying SME [31–34]. Volume expansion of 4–5% and shear strain of 14–15% occur during the phase transformation [35]. For pure ZrO_2, the transformation $t \rightarrow m$ occurs at $\sim$ 950 °C, whereas the reverse transformation $m \rightarrow t$ occurs at $\sim$ 1170 °C. By modifying zirconia with other oxides, for example, ceria and yttria, the transformation temperatures (T_T) can be tuned and t-ZrO_2 can be stabilized at room temperature [17, 36].

The SME of ZrO_2 was first observed in magnesia-partially-stabilized-zirconia (MgO-PSZ) ceramics [37]: a bent MgO-PSZ bar recovered its shape upon heating above 800 °C. The reversible deformation strain is only 0.5%, limited by the brittleness of the bulk ceramic. The precipitates of t-ZrO_2 in the c-ZrO_2 matrix undergo the martensitic transformation. Morel et al. reported PE and SME in CeO_2-stabilized tetragonal zirconia polycrystals (Ce-TZP) containing 12 mol% CeO_2 [17]. The as-sintered ceramics were entirely t-ZrO_2 with grain sizes of $\sim$ 1–2.8 μm. Upon loading at room temperature, a plastic deformation up to 1% occurs due to the $t \rightarrow m$ phase transformation. The strain remains after the load is removed. Subsequent heating above 186 °C results in the recovery of approximately 95% strain because of the reverse $m \rightarrow t$ phase transformation. Zhang et al. studied the SME of ZrO_2 samples with different contents of CeO_2 (8–12 mol%) and Y_2O_3 (0.25–0.75 mol%) and found that the 8Ce–0.50Y–TZP shows a recoverable strain of $\sim$ 1.2% and no micro-cracks were found after shape recovery [38]. As mentioned, ZrO_2 SMO can be used for applications where SMA is not applicable, such as high-temperature devices in oxidative environment. However, its practical application is limited by the relatively low recoverable strain and tendency of micro-cracking.

SME of ZrO_2 at Small Scales

Methods that have been used in SMAs research (Sect. 2) were considered to be used to explore and achieve higher strains without micro-cracks in ZrO_2 ceramics during the phase transformation [27, 28, 39]. Different forms of ZrO_2 in small scale have been proven to show excellent SME, i.e., submicrometer pillars [18], micro-particles [40], granular packing [41], foam [42], as summarized in Fig. 2. The aim of small-scaling is to reduce the mismatch stress at grain boundaries and increase the surface area to relax the stress during the martensitic transformation.

The concept was first tried on micrometer-scale pillars fabricated from polycrystalline Ce-/Y-ZrO_2 by Lai et al. using focused ion-beam (FIB) milling [18]. Each micropillar can be viewed as a single crystal or oligocrystal as the size of the micropillar is designed to be smaller than or close to the average grain size of the ceramic. In the stress–strain curve of a 16 mol% CeO_2–ZrO_2 loaded in compression (Fig. 2a), the austenite phase first undergoes a linear elastic deformation with loading. At a critical stress, the phase transformation to the martensite phase is induced, indicated by plateaus and reduced slope in the curve. The transformation shows a large strain of 7% and was reversed upon unloading. The reversion of the transformation remains after dozens of cycles. SME was also observed from the micropillar accompanied with a large recoverable strain of 8%. A load in bending mode was applied to a pillar of 8 mol% CeO_2–0.5 mol% Y_2O_3-ZrO_2. Upon loading, the austenite pillar undergoes stress-induced

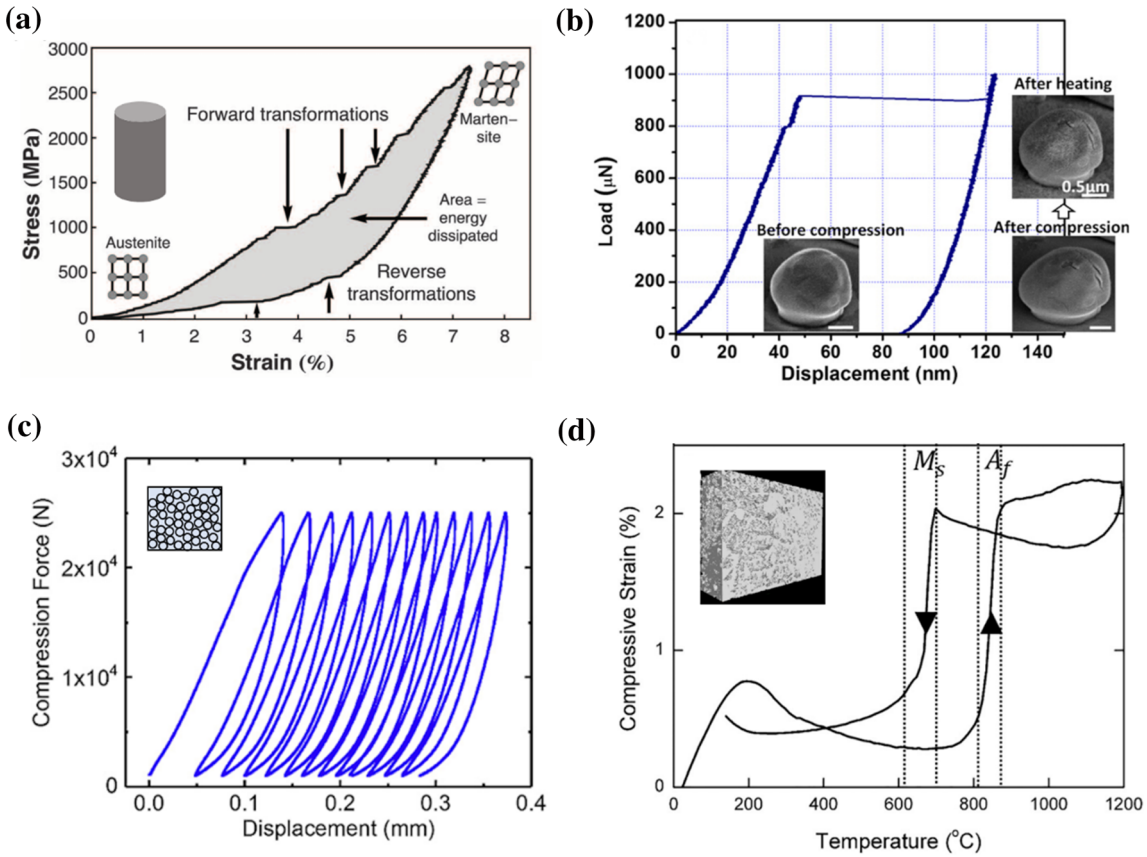

Fig. 2 SE/SME manifested in different forms of small-scale ZrO_2 SMO: **a** Micro-compression stress–strain curve for 16 mol% CeO_2–ZrO_2 pillar with effective diameter d_{eff} = 1.82 μm, in which the initial elastic loading of austenite is followed by forward transformation plateaus during the formation of martensite. Reversion to austenite is observed during unloading. "Reprinted from Reference [18] with permission, Copyright (2013), The American Association for the Advancement of Science." **b** Load–displacement curves of 14 mol% CeO_2–ZrO_2 particles. Inset SEM images show the particle before and after compression and after heating. "Reprinted from Reference [40] with permission, Copyright (2017), John Wiley and Sons." **c** Load–displacement curves of 300 mg $(ZrO_2)_{0.85}$-$(CeO_2)_{0.15}$ powders (tetragonal phase) under cyclic loading from 35 to 880 MPa. "Reprinted from Reference [41] with permission, Copyright (2017), Elsevier." **d** Curves of 6 mol% Ce–zirconia foam where transformation temperatures are in line with dimensional changes. "Reprinted from Reference [42] with permission, Copyright (2017), Elsevier"

transformation and forms a new shape in the martensite phase, which remains after unloading. By heating the bent pillar above A_F, the transformation is reverted, and the shape of the pillar is recovered.

Further investigations on the size dependence of recoverable strain of fine-scale pillars indicates the advantage of the oligocrystalline structure with less grains, grain boundaries and triple junctions [43]. Micropillars with diameters ranging from 0.7 to 3.0 μm were fabricated by FIB from 8 mol% CeO_2–0.5 mol% Y_2O_3–ZrO_2 with average grain size of 1.7 μm. When the pillar diameter is smaller than the average grain size of the ceramic, the pillar shows significant strains from 3 to 8% during the phase transformation, without fracture. In contrast, larger pillars with diameters above 2 μm tend to fracture and show smaller strains.

As the martensitic transformation of zirconia between tetragonal and monoclinic phases is highly anisotropic, the transformation stress and strain are dependent on the crystallographic orientation. Study on the stress-induced martensitic transformation of ZrO_2 macro-pillar suggests that the critical stress at which transformation occurs is orientation-dependent (Fig. 3) [44]. Not only phase transformation but also fracture and slip were observed during the compression test. For instance, the orientations near [001] and [100] require large stress for transformation and as a result fracture occurs before the transformation is triggered. While for orientation near [110], the crystal slip is favored and observed upon loading. Therefore, in practical application of SMOs, the control of orientation or texture is very important to obtain desired SME or SE performance.

The SME of zirconia micro-particles was also studied [40]. Spherical Ce-ZrO_2 with diameters in the range of 0.8–3.0 μm were synthesized by sol–gel method. The Ce–ZrO_2 single-crystal particles showed excellent SME and SE

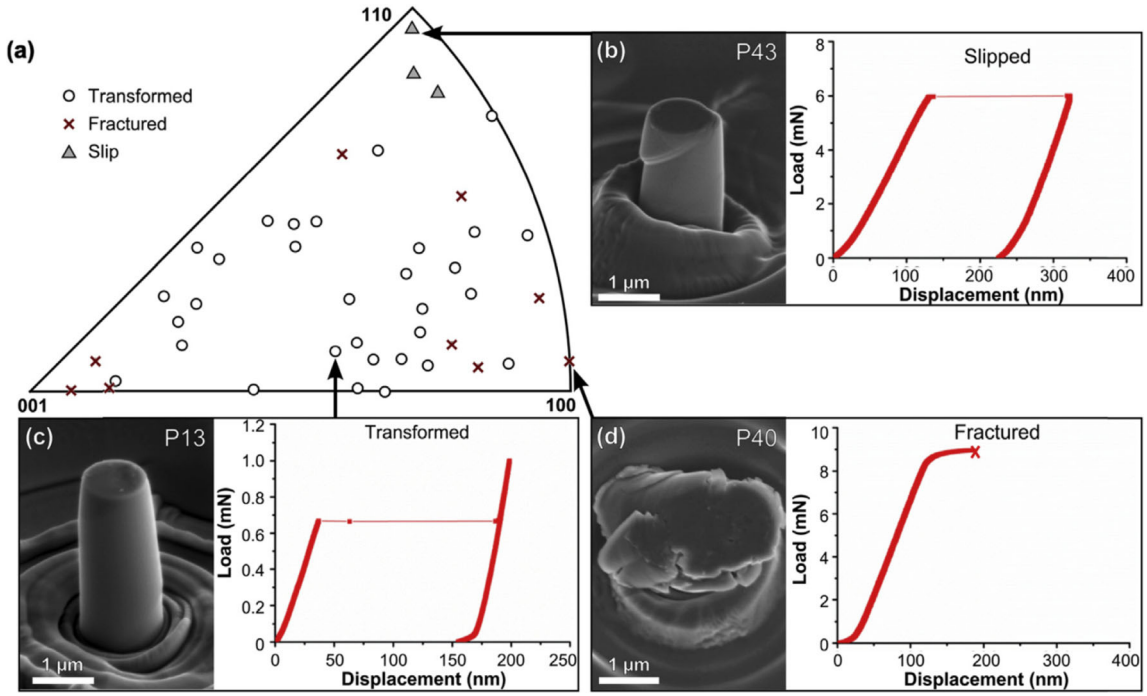

Fig. 3 **a** Crystal orientations of pillars on a tetragonal standard stereographic triangle, with typical load–displacement curves and corresponding the as-deformed pillar morphology for pillars that **b** slipped, **c** transformed and **d** fractured. "Reprinted from Reference [44] with permission, Copyright (2016), Elsevier"

properties with recoverable strain up to 4.7% (Fig. 2b). The shape memory particle containing 16 mol% ceria exhibited highly reproducible SE through over 500 load cycles.

The unveiled excellent SME and SE of ZrO_2 in small-scale structures enables the development of, e.g., actuators with high work density, high energy damping and high-temperature range. For instance, work density of the SMO is determined on the order of 100 MJ/m^3, which is higher than that of SMA and hydraulics. The large hysteresis area of the stress–strain loop of the small-scale ZrO_2 provides a merit index of damped energy on the level of $\sim$ 2 GPa$^{1/2}$, which is two times larger as that of Cu–Al–Ni microscale SMA.

Among small-scale forms, granular packing and foam are promising for bulk applications. The SME of granular packed Ce–ZrO_2 was studied by Yu et al. [41], in which particles of 3 μm or smaller were compacted and compressed. The particles were obtained by fine grinding from particles with grain size ranging up to 10 μm, which can be considered as single- or oligocrystalline. A reversible martensitic transformation was triggered by uniaxial compression, during which a remarkably high energy dissipation of $\sim$ 2 J/g was obtained. Compared to the martensitic transformation of micropillars, the volume fraction of granular packed materials which go through the stress-induced transformation is limited to 25–40%, due to non-uniform stress distribution in powder compaction. However, aggregation of the granular SMO packing provides a possible method toward bulk-level application, such as energy dissipation and damping. Another form of small-scale SMO toward bulk application is foam SMO [42], in which micro-pores and -struts are capable to exhibit SME due to the fine scale. An open-cell foam of Ce-ZrO_2 exhibited recoverable strain of $\sim$ 2% through multiple cycles, which is higher than that of its polycrystalline bulk counterpart.

Recently, nanofiber-based yarns and springs made from $8CeO_2$–$0.5Y_2O_3$–ZrO_2 were fabricated by electrospinning, which show a recoverable strain of up to 5% with short recovery time of 0.16 s at temperature of 328–388 °C [45]. The output stress, work density of the yarns and springs exhibited during the shape memory actuation are 14.5–22.6 MPa and 15–20 kJ/m^3, which are higher than those of human muscles and some polymer-based artificial muscles. Given the high actuation temperature and chemical resistance of SMO, nanofiber-based yarns and springs are excellent candidate for artificial muscle used in extreme environment.

Other forms of ZrO_2, e.g., thin films, which have not been reported yet, could also be of research interest, since it is in principle possible to have single-crystalline or oligocrystalline structures, which could lead to better SME/SE than bulk materials.

In general, the excellent SME/SE performances mentioned above are related to the small-scaling at the level of up to a few microns, based on the approach of eliminating grain boundaries. A recent study by Crystal et al. [46] takes a step further by extending the strategy to mm-scale bulk size, in which mm-scale zirconia single crystals withstand cyclic martensitic transformation through 125 cycles without obvious degradation of the strain amplitude of ~ 3% and cracking. In comparison, the strain of a large zirconia polycrystal sample during the cyclic martensitic transformation is reduced to 1.5% after 10 cycles, and a large specimen mass loss of 35% was observed after 45 cycles due to the cracking. Those results confirm that controlling the grain boundaries in the SMO will significantly affect its SME/PE performance, not only at microscale but also at mm-scale.

SME in Ferroelectrics

Due to the existence of crystalline structures of different symmetry such as cubic, tetragonal and rhombohedral in perovskite ferroelectric oxides, the SME can also be observed, which is associated with paraelectric (PE)-ferroelectric (FE) and antiferroelectric (AFE)-FE phase transformations. Upon applying electric field, the reorientation of polar domains occurs during the phase transformation.

Compared to the SME of SMAs, the recoverable strain of ferroelectrics is much lower, in general < 1%. However, driven by electric field, the response speed of the ferroelectrics is much faster, which makes shape memory ferroelectrics interesting for applications. Numerous investigations have been carried out [16, 47–60]. For example, in the system $Pb_{0.99}Nb_{0.02}[(Zr_{0.6}Sn_{0.4})_{1-y}Ti_y]_{0.98}O_3$ (PNZST), the SME is observed through the transformation between high-temperature AFE and low-temperature FE [16]. (Pb,La)(Zr,Sn,Ti)O_3 (PLZST) tetragonal antiferroelectric single crystals show a large electric field-induced strain up to 0.76% at 110 °C [55].

Due to the toxicity of Pb, investigation on Pb-free ferroelectric systems has drawn interest. Aged $BaTiO_3$ was reported to exhibit an electro-induced nonlinear strain of 0.75% at a field of 200 V/mm (Fig. 4), which is 40 times higher than the piezoelectric response in Pb(Zr, Ti)O_3 (PZT) ceramics and more than 10 times higher than the strain in $Pb(Zn_{1/3}Nb_{2/3})O_3$–$PbTiO_3$ (PZN-PT) single crystals at the same field [50]. The large strain is attributed to reversible domain switching and the restoring force was proposed to be a general symmetry-conforming property of point defects.

The multiferroic material BFO is of great interest because its properties include ferroelectricity and ferromagnetism [61, 62]. Bulk BFO has a low-symmetry

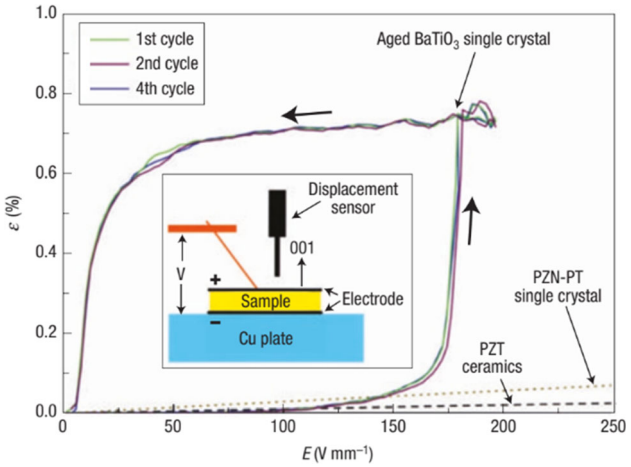

Fig. 4 Large recoverable electric field-induced strain in an aged $BaTiO_3$ single crystal along the [001] pseudo-cubic direction, in comparison with the piezoelectric effect of soft PZT ceramics and PZN-PT single crystals (dash lines). Inset is the set-up for displacement measurement, which used an optical displacement sensor (non-contact) to measure the strain from the free upper electrode in order to exclude the possible constraint/clamping effect. "Reprinted from Reference [50] with permission, Copyright (2004), Springer Nature"

rhombohedral structure with space group R3c. By strain-engineering, tetragonal variant of BFO was fabricated, and thermal-/electrical-induced martensitic-like transformation of BFO from rhombohedral (R) phase to tetragonal (T) phase was observed. The recoverable strain during the transformation is up to 14%, which is significantly larger than that exhibited by its bulk ceramic counterpart of 0.36% associated with domain switching [19, 58]. This discovery suggests the importance of strain-engineering and small scale in achieving high-performance electromechanical response in ferroelectric materials. In the following section, details about the investigations on nanoscale BFO are summarized.

SME of Nanoscale BFO

Although the ground state of BFO is the rhombohedral structure (R), it was reported that BFO thin films can be stabilized in a tetragonal phase (T) by epitaxial strain [63]. Epitaxially grown on single-crystal substrates of (001) $LaAlO_3$ (LAO) and (110) $YAlO_3$ (YAO) using molecular beam epitaxy, BFO films of different phases can be obtained due to varied strain levels at the interface induced by lattice mismatch. At high-strain level (high compressive strain on YAO), T phase was stabilized. In contrast, for the film grown on LAO (less compressive strain), R phase emerges as the film becomes thicker and the strain is relaxed, which leads to an outcome of T/R phase mixture on a nano level.

Figure 5a shows the phase diagram of a BFO thin film with respect to temperature and strain [63], illustrating the strain-driven morphotropic phase boundary (MPB) in BFO. MPB refers to phase transitions between tetragonal and the rhombohedral ferroelectric phases with respect to varied composition or mechanical pressure. In perovskite-type ferroelectrics, excellent electromechanical performance is usually shown in the vicinity of MPB [48, 64–67]. Similarly, T/R nanoscale phase mixture in BFO turns out to show excellent electromechanical response. By applying electric field or mechanical force, reversible transformation between T/R mixture phase and pure T or R phase has been achieved [68]. The accompanying reversible strain of $\sim$ 5% is higher than that of traditional ferroelectric materials. Those results suggest that the MPB of BFO could also be affected by the electric field and stress that are applied to the material, in addition to the composition and the misfit strain of the material. Moreover, it was inferred that phase transformation directly between T and R phase, if possible, has the potential for larger strain.

A large recoverable strain of $\sim$ 14% for nanoscale BFO was reported by Zhang et al. [19]. In their study, pure R

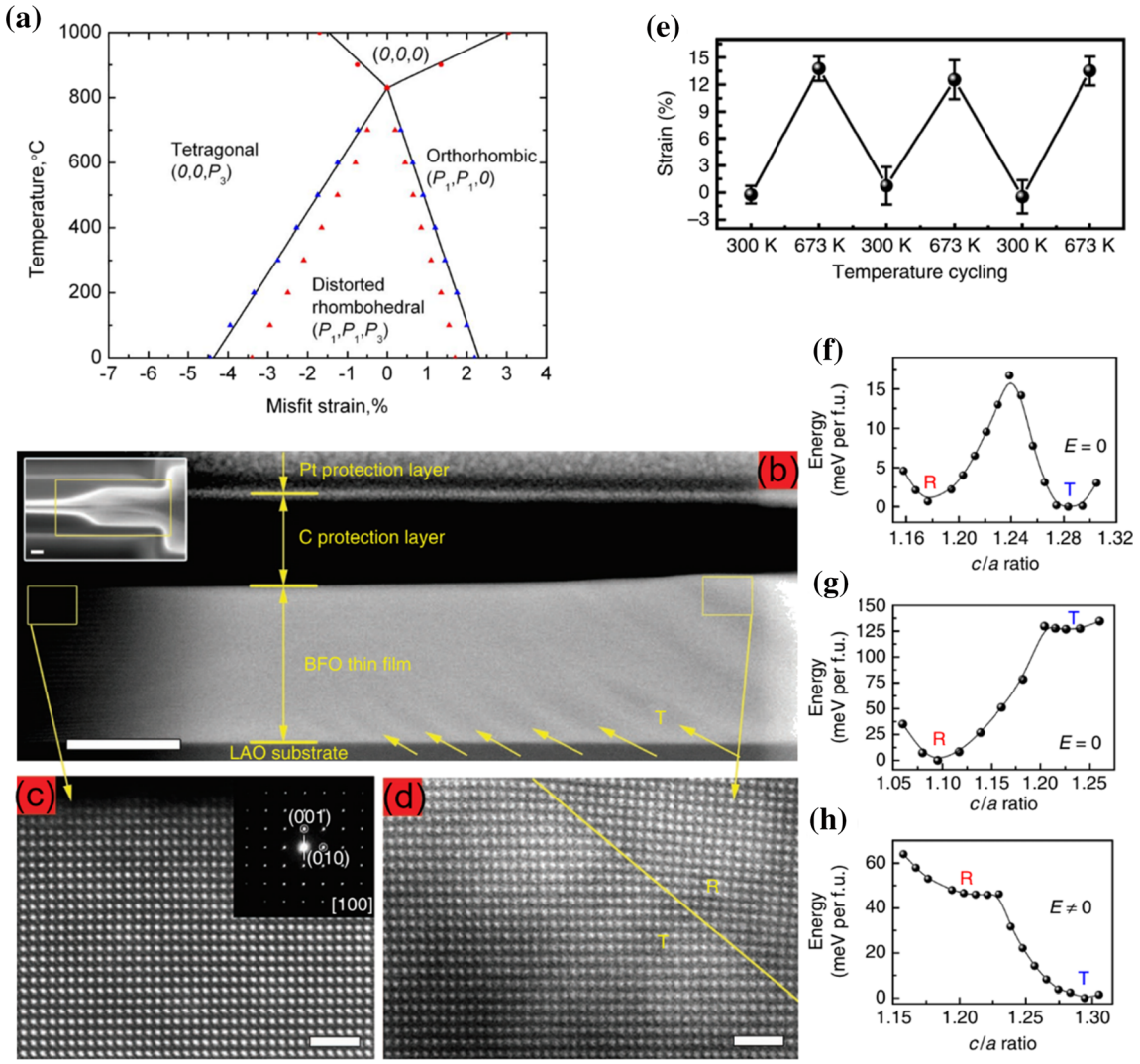

Fig. 5 SME in nanoscale BFO. **a** Calculated phase diagram of BFO as a function of temperature and misfit strain. Different phases are labeled in the diagram, in which (0,0,0) on the top denotes the cubic paraelectric phase. "Reprinted from Reference [63] with permission, Copyright (2009), The American Association for the Advancement of Science." **b–d** TEM images to confirm the variation of the BFO phase from a mixed phase to pure R phase with reduced clamping, in which, **b** shows a cross-sectional HAADF-STEM images from a wedge-shaped lamella. Inset is the film top view to show the wedge shape. **c**, **d** are high-resolution TEM images of the film from pure R and mixed phase area. **e** Reversible strain from the transformation between R and T phases during temperature cycling. The sample for the test is from pure R phase area in (**b**). **f–h** The transformation is studied by first-principles calculations, and the evolutions of energy as a function of *c*/*a* ratio are presented under different conditions: **f** 5.8% strain, **g** 4% strain, **h** a homogeneous electric field of 0.2 V/nm along [001] direction. "Reprinted from Reference [19] with permission, Copyright (2013), Springer Nature"

phase BFO was obtained from the as-deposited T/R phase mixture grown on LAO by reducing the clamping of the film from the substrate, which was achieved by reducing the lateral size of the film using FIB milling. It has been estimated that the clamping starts to decrease for lateral dimensions around 10 μm and is mostly removed around 1 μm. The T phase proportion in the T/R phase mixture decreases with lateral size until it completely disappears, which was indicated by the change of the surface topography. Direct identification of the stabilized phase in the film with less constraint was performed by TEM (Fig. 5), in which a thin cross-sectional sample with wedge shape area with thickness varying from 300 to 50 nm confirmed the structural change from R/T mixed phase to a pure R phase with substrate clamping removed.

Upon heating, pure R phase BFO starts to transform to T phase at 573 K and the phase transformation was completed at 673 K. Temperature cycling exhibited an average recoverable strain of $\sim 12 \pm 2\%$. In addition, large reversible SME in the unconstrained structure can also be driven by electric field of 1–2 MV/cm at room temperature. Moreover, the phase stability and transformation of BFO with respect to strain and electric field are interpreted by first-principles calculations. Calculated energy of BFO as a function of c/a ratio was studied at different stress and electric field conditions (Fig. 5). Under a strain of $-$ 5.8%, there are two energy minima corresponding to the stable R and T phases, which suggested the coexistence of the phases. At smaller compressive strain, the R phase is energetically favorable, which reflected the transformation from T phase to R phase in the milled film. In the presence of electric field, the T phase showed much lower energy, which is in favor of the electric-induced phase transformation. It is noteworthy that T phase has a significantly higher energy than R phase under a strain-relaxed state, which makes the transition from R to T phase very difficult. Therefore, presence of suitable clamping stress in the BFO thin film seems to be important for the phase transformation to occur.

In summary, the large SME behavior of BFO in nanoscale originates from the structural phase transformation, which is driven by the interplay between stress, electrical field and temperature. Given the high Young's Modulus of the material, the SME of BFO could provide a volumetric work density of 600 J/cm^3, which is of great potential for applications in nanosystems.

VO_2

VO_2 undergoes a metal–insulator transition (MIT) at a critical temperature T_c of 68 °C, accompanied by crystalline structure change from rutile (R) to monoclinic (M) phase. Rutile VO_2 (R) belongs to the crystallographic group P42/mnm, with a = b = 0.455 nm, c = 0.285 nm, in which a V atom is surrounded by an octahedron of O atoms. Along the c_R axis, V atoms are equally positioned with a distance of 0.288 nm. The monoclinic VO_2 (M1) phase belongs to the crystallographic group P21/c, with a = 0.575 nm, b = 0.452 nm, c = 0.538 nm, β = 122.6°. V atoms pair along the rutile c axis in zigzag type, with alternative distances of 0.312 nm and 0.265 nm [69].

Along the transformation from M phase to R phase, the unit cell of VO_2 expands by $\sim$ 0.32% (one unit cell of M phase consists of two unit cells of R phase) and the area for (011) M and (110) R planes is decreased by 1.7%, resulting in a strain of up to 1% along the rutile c axis. Because of high Young's modulus E of VO_2 ($\sim$ 140 GPa), high volume work density, given by $E^*\varepsilon^2/2$, is expected associated with the phase transition, which could be used for micro-/nanoactuators [70]. Apart from the M1 to R phase transformation, it was reported that another monoclinic phase of VO_2 (M2) shows higher strain ($\sim -$ 1.7%) across its transformation into R phase [71]. M2-based actuators tend to exhibit a higher work density. M2 is a metastable phase of VO_2, which can be stabilized by either applying stress along c_R [72] or adding trivalent ions such as Fe^{3+}, Cr^{3+} and Al^{3+} [73–75]. In addition, the electrical and optical properties of VO_2 change during the phase transition, which makes VO_2 interesting as a multifunctional material. In this section, we review research on the mechanical response of VO_2 as well as studies on the stress change of VO_2-based thin film materials libraries.

Mechanical Response of VO_2

The mechanical response of VO_2 is mainly studied in the form of thin films, since the thin film is able to withstand the volume change during the phase transformation cycling without fracture. For instance, a VO_2-coated microcantilever was fabricated and studied by Rúa et al. [70], where 240 nm thick VO_2 film was deposited by pulsed laser deposition (PLD) on Si microcantilever with dimensions of 130 μm long, 35 μm wide and 1 μm thick. The deflection of the cantilever was recorded by CCD camera at different temperatures (Fig. 6a) and a curvature change of over 2000 m^{-1} was observed at the temperature range where phase transition of VO_2 occurs, which results in recoverable stress of $\sim$ 1 GPa. It is noteworthy that strain of VO_2 in the microcantilever is about 0.3%, smaller than theoretical value, which is limited by the polycrystalline characteristic of VO_2 used in the study. With randomly oriented grains, the strain from c_R-oriented grains is compensated to some extent by that from a_R- and b_R-oriented grains because of the opposite directions of those strains.

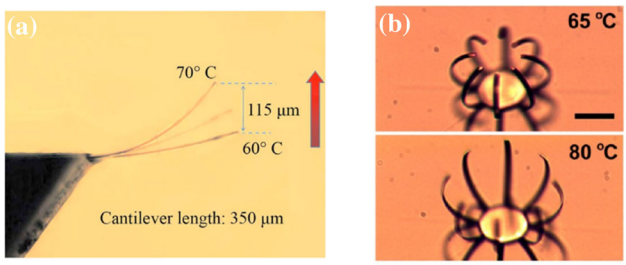

Fig. 6 SMEs in VO_2-based cantilevers: **a** deflection of a single VO_2-coated Si cantilever. "Reprinted from Reference [70] with permission, Copyright (2010), AIP Publishing." **b** A balm-structure microactuator made of Cr/VO_2 bimorphs. The actuator can open and close at different temperature because of the curvature change during the phase transformation. "Reprinted from Reference [80] with permission, Copyright (2012), American Chemical Society"

In contrast, a microcantilever made of single-crystal VO_2 exhibits colossal thermal–mechanical actuation [76]. Single-crystal VO_2 microbeams grown along c_R axis were coated with Cr to form bilayer cantilevers. The curvature change of the cantilever is about 4000/m K as the phase transformation occurs, which is 10 times higher that of the polycrystalline VO_2/Si cantilevers. The work density of single-crystal VO_2 is theoretically 7 J/cm^3, using E of 140 GPa and strain of 1%, which is comparable to that of SMAs and more than one order of magnitude higher than that of electrostrictive polymer. Moreover, a study was performed on $V_{0.976}Cr_{0.024}O_2$-coated (VO_2 M2) cantilevers to investigate the phase transformation from R to M2. It was reported that the VO_2 M2-coated cantilever shows larger curvature change of 2900 m^{-1}, in comparison to 1850 m^{-1} for a VO_2-coated cantilever [77].

Researches on VO_2-based actuators have also been carried out. For instance, electro-thermally driven VO_2-based actuators were studied, which consist of SiO_2, Ti/Pt metal electrode/heater layers and a VO_2 active layer [78, 79]. The top Pt layer serves as an integrated heater for the actuator. The VO_2 layer of 200 nm thickness was fabricated by PLD. The final thickness of the cantilever is about 1 μm. By Joule heating, total deflections of 68.7 and 28.5 μm were observed for 300 and 200 μm long cantilevers, respectively. It was found that the current needed for maximum deflection is dependent on the ambient conditions, and power needed for triggering the phase transition of VO_2 is significantly smaller when operated in vacuum than in air. The cut-off frequency (f_{3dB}) of the 300 μm long actuator operated in vacuum is 29 Hz, whereas it is 541 Hz when operated in air because of strong convection heat losses.

Similar VO_2-based actuators were also fabricated and studied by Liu et al. [80]. Cr/VO_2 bimorph actuators were fabricated with the thickness of VO_2 in the nanoscale ranging from 100 to 300 nm. Figure 6b shows the optical images of bending Cr/VO_2 cantilevers at two temperatures across phase transition. It was observed that the Cr/VO_2 bimorph actuators exhibit high displacement-to-length ratio, which is one important performance of microscale actuation. A palm structure made of many Cr/VO_2 bimorph cantilevers works as a thermally driven microactuator. By varying temperature from room temperature to 80 °C, the palm can repeatedly open and close, which might be used to capturing and releasing objects at microlevel. The actuators show work density over 0.63 J/cm^3 at frequencies up to 6 kHz in both ambient and aqueous conditions.

Transition Properties Tuning in V–M (Metal)–O Libraries

The advantages such as the superior performance and microscale manufacturability make the VO_2-based actuator promising applications in microelectromechanical systems [80]. An even more beneficial aspect of such an actuator is

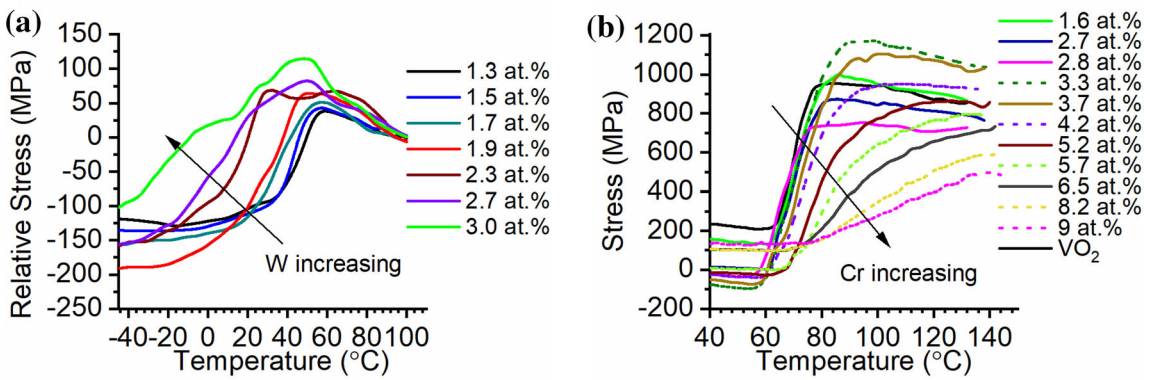

Fig. 7 The temperature-dependent stress change of **a** V–W–O libraries with different W contents. The stress change was normalized to the stress at 100 °C. "Reprinted from Reference [84] with permission, Copyright (2018), American Chemical Society." **b** V–Cr–O libraries with different Cr contents. "Reprinted from Reference [85] with permission, Copyright (2020), American Chemical Society"

Table 1 Summary of the shape memory effects of different materials

Materials	Transformation temperature range (°C)		Recoverable strain (%)	Comment
	M_f	A_f		
Bulk NiTi [4, 8]	− 100 to 100		~ 8	Transformation temperature depends on the composition and processing history
Nanocrystalline NiTi [20]	23	88	–	The martensitic phase transformation is strongly suppressed upon decreasing grain size less than about 100 nm. In nanograins smaller than a critical size of 50 nm, the transformation is completely suppressed
Cu–Al–Ni microwires [26]	0	40	~ 6.8	Diameter of the microwire is 90 μm
12 mol% CeO_2–ZrO_2 [17]	− 31	186	~ 1	–
8 mol% CeO_2–0.50 mol%Y_2O_3–ZrO_2 [18, 38]	–	430	~ 1.2	–
16 mol% CeO_2–ZrO_2 micropillar [18]	–	0	~ 7	The pillar diameter is 1.82 μm
14 mol% CeO_2–ZrO_2 particles [40]	–	179	~ 4.7	The particle diameter is 1.64 μm
15 mol% CeO_2–ZrO_2 granular packing [41]	–	≤ 25	–	Particle size is 3 μm or below. High energy dissipation of ~ 2 J/g was obtained during phase transformation
6 mol% CeO_2–ZrO_2 foam [42]	642	868	~ 2	–
Bulk $BaTiO_3$ [50]	–	–	~ 0.75	Electric field-induced phase transformation at a low field of 200 V/mm
Nanoscale $BiFeO_3$ [19]	–	400	~ 14	The phase transformation can be induced by electric field of 1–2 MV/cm at room temperature
VO_2 thin film [70]	~ 68		~ 0.3	The transformation temperature is changed by adding other elements or applying stress
VO_2 single crystal [76]	~ 68		~ 1	–

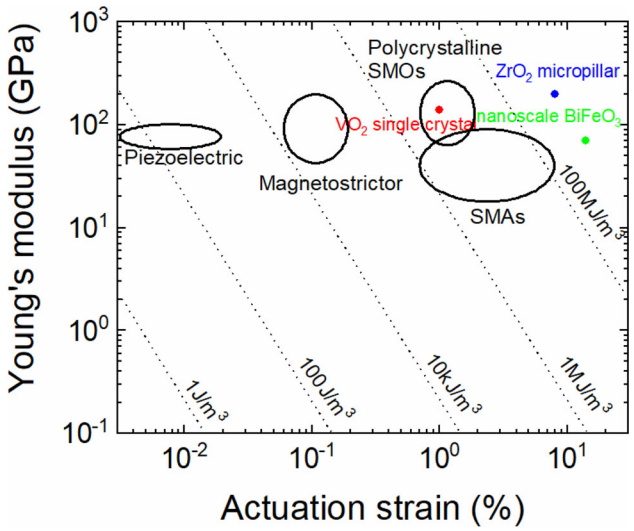

Fig. 8 Young's modulus and actuation strain for various actuator materials and systems. Contours of constant specific work density are indicated by dashed lines. Data for high-strain piezoelectric ceramics, magnetostrictive materials, SMAs are summarized from elsewhere [86]. The performances of the small-scale SMOs are marked as dots with colors (Color figure online)

that its performance could be flexibly modified by tuning the phase transformation properties of the active layer VO_2. For example, T_c can be influenced by the addition of third elements to VO_2: e.g., it is increased by addition of Cr [77], Ti [81], whereas it is decreased by W [82] and Mo [83]. It is likely that the mechanical response of VO_2 across the IMT is also influenced, considering structural distortions induced by the addition of a third element. Transition properties tuning, including T_c and stress change of V–M–O were studied by combinatorial depositions and high-throughput characterizations.

In V–W–O libraries [84], it was observed that when W content x in $V_{1-x}W_xO_2$ increases from 0.007 to 0.044 the crystalline structure gradually shifts from the VO_2 (M) phase to the VO_2 (R) phase. Meanwhile, T_c was decreased by 15 K/at.% W, accompanied with a wider transition range and a narrower hysteresis with a minimal value of 1.8 K. To study the mechanical response of $V_{1-x}W_xO_2$, a library was deposited on a Si_3N_4/SiO_2-coated Si cantilever array wafer. The temperature-dependent stress change σ (T) of films with different W content through the phase transition was measured (Fig. 7a). Compared with σ

(T) of $\sim$ 700 MPa of a VO_2 film, σ (T) in $V_{1-x}W_xO_2$ films decreases to $\sim$ 250 MPa. Meanwhile, σ (T) becomes less abrupt and occurs over a wider temperature range with decreased transition temperatures.

In V–Cr–O libraries [85], gradual changes in the crystalline structures of VO_2 were observed in the thin film libraries at room temperature as the M1 phase exists for Cr < 1.2 at.%, the M2 phase for Cr > 4.2 at.% and an intermediate T phase in between. T_c was increased by 4.9 K/at.% in the composition range 2.8 at.% < Cr < 7.3 at.% and 1.2 K/at.% for Cr > 7.3 at.%. V–Cr–O libraries were deposited on stress sensor to study their stress change. High-throughput stress ($\sigma(T)$) measurements (Fig. 7b) indicate that the addition of Cr increased the stress change across the phase transformation up to 1.3 GPa for a Cr content of 3.3 at.%. It was found that the mechanical performance of V–Cr–O is also affected by fraction of other oxide and crystallographic orientation. As a result, the stress change of V–Cr–O library decreased to 380 MPa with Cr contents increased from 3.3 at.% to 9 at.%.

Summary and Outlook

Comparisons between SMAs and SMOs are presented in Table 1 and Fig. 8. SMOs at small scale show excellent mechanical response during the phase transformation: Ce-ZrO_2 micropillars show large strain of up to 7% upon compression loading, nanoscale $BiFeO_3$ thin films with clamping removed can achieve a maximum strain of up to 14%, VO_2 single-crystal actuator of small scale has the potential of providing high work density comparable to SMAs. Compared to the SMAs, ZrO_2 and BFO at small scale are capable to exhibit even higher work density as actuator.

Small-scaling provides a new path for SMOs to exhibit better mechanical response than that of their bulk counterparts. For ZrO_2, small-scaling primarily reduces the grain boundary volume in the material and facilitates the formation of oligocrystalline/single-crystalline structure, which significantly eliminates the constraint and mismatch stress during the martensitic transformation. For $BiFeO_3$, small-scaling associated with strain-engineering stabilizes pure phase instead of mixed phase in the vicinity of MPB. As a result, the largest strain is achieved in BFO via the phase transformation from pure T to pure R phase. For VO_2, the mechanical response during the phase transformation is well exhibited in the form of thin film or thin film based microcantilever/actuators.

Small-scale SMOs could have promising prospects in many applications such as MEMS, energy damping, because of their superior mechanical performance. Meanwhile, similar methodology might be applied to other SMOs to modify their mechanical response. By small-scaling and strain-engineering, the amount of grain/domain boundaries can be reduced to relax the transformation constraint. Moreover, with tuning the phase boundaries (MPB in ferroelectrics systems) in the complex phase diagram of SMOs, for example, by varying the content of the second oxide in ZrO_2 system and by changing the content of M in the V–M–O system, new transformation performance might be explored.

Acknowledgements Open Access funding provided by Projekt DEAL. This work was supported by the German Research Foundation (DFG), Project Number LU 1175/18-1.

References

1. Jani JM, Leary M, Subic A, Gibson MA (2014) A review of shape memory alloy research, applications and opportunities. Mater Des 56:1078–1113
2. Wei ZG, Miyazaki S (1998) Shape-memory materials and hybrid composites for smart systems: part I shape-memory materials. J Mater Sci 33:3743–3762
3. Qiu Y, Young ML, Nie X (2015) Influence of dynamic compression on phase transformation of martensitic NiTi shape memory alloys. Metall Mater Trans A 46(10):4661–4668
4. Shaw JA, Kyriakides S (1995) Thermomechanical aspects of NiTi. J Mech Phys Solids 43:1243–1281
5. Humbeeck JV (1999) Non-medical applications of shape memory alloys. Mater Sci Eng A 273–275:134–148
6. Kahn H, Huff MA, Heuer AH (1998) The TiNi shape-memory alloy and its applications for MEMS. J Micromech Microeng 8(3):213–221
7. Prokoshkin S, Brailovski V, Dubinskiy S, Zhukova Y, Sheremetyev V, Konopatsky A, Inaekyan K (2016) Manufacturing, structure control, and functional testing of Ti–Nb-based SMA for medical application. Shap Mem Superelasticity 2(2):130–144
8. Duerig T, Stoeckel D, Johnson D (2003) SMA: smart materials for medical applications. Proc. SPIE 4763, European Workshop on Smart Structures in Engineering and Technology
9. Stoeckel D (1990) Shape memory actuators for automotive applications. Mater Des 11(6):302–307
10. Hartl DJ, Lagoudas DC (2007) Aerospace applications of shape memory alloys. J Aerosp Eng 221(4):535–552
11. Waitz T, Kazykhanov V, Karnthaler HP (2004) Martensitic phase transformations in nanocrystalline NiTi studied by TEM. Acta Mater 52(1):137–147

12. Waitz T, Tsuchiya K, Antretter T, Fischer FD (2009) Phase transformations of nanocrystalline martensitic materials. MRS Bull 34:814–821
13. König D, Naujoks D, los Arcos TD, Grosse-Kreul S, Ludwig A (2015) X-ray photoelectron spectroscopy investigations of the surface reaction layer and its effects on the transformation properties of nanoscale $Ti_{51}Ni_{38}Cu_{11}$ shape memory thin films. Adv Eng Mater 17(5):669–673
14. Zaeem MA, Zhang N, Mamivand M (2019) A review of computational modeling techniques in study and design of shape memory ceramics. Comput Mater Sci 160:120–136
15. Motemani Y, Buenconsejo PJS, Ludwig A (2015) Recent developments in high-temperature shape memory thin films. Shap Mem Superelasticity 1(4):450–459
16. Uchino K (2016) Antiferroelectric shape memory ceramics. Actuators 5(2):11–33
17. Reyes-Morel PE, Cherng JS, Chen IW (1988) Transformation plasticity of CeO_2-stabilized tetragonal zirconia polycrystals: II, pseudoelasticity and shape memory effect. J Am Ceram Soc 71(8):648–657
18. Lai A, Du Z, Gan CL, Schuh CA (2013) Shape memory and superelastic ceramics at small scales. Science 341(6153):1505–1508
19. Zhang J, Ke X, Gou G, Seidel J, Xiang B, Yu P, Liang WI, Minor AM, Chu YH, van Tendeloo G, Ren X, Ramesh R (2013) A nanoscale shape memory oxide. Nat Commun 4:2768–2778
20. Waitz T, Antretter T, Fischer FD, Karnthaler HP (2008) Size effects on martensitic phase transformations in nanocrystalline NiTi shape memory alloys. Mater Sci and Technol 24(8):934–940
21. San Juan J, Nó ML, Schuh CA (2009) Nanoscale shape-memory alloys for ultrahigh mechanical damping. Nat Nanotechnol 4(7):415–419
22. Gómez-Cortés JF, Nó ML, López-Ferreño I, Hernández-Saz J, Molina SI, Chuvilin A, San Juan J (2017) Size effect and scaling power-law for superelasticity in shape-memory alloys at the nanoscale. Nat Nanotechnol 12:790–796
23. Frick CP, Orso S, Arzt E (2007) Loss of pseudoelasticity in nickel–titanium sub-micron compression pillars. Acta Mater 55:3845–3855
24. Ye J, Mishra RK, Pelton AR, Minor AM (2009) Direct observation of the NiTi martensitic phase transformation in nanoscale volumes. Acta Mater 58:490–498
25. Clark BG, Gianola DS, Kraft O, Frick CP (2010) Size independent shape memory behavior of nickel-titanium. Adv Eng Mater 12:808–815
26. Chen Y, Zhang X, Dunand DC, Schuh CA (2009) Shape memory and superelasticity in polycrystalline Cu–Al–Ni microwires. Appl Phys Lett 95(17):171906
27. Ueland SM, Chen Y, Schuh CA (2012) Oligocrystalline shape memory alloys. Adv Funct Mater 22(10):2094–2099
28. Chen Y, Schuh CA (2011) Size effects in shape memory alloy microwires. Acta Mater 59(2):537–553
29. König D, Buenconsejo PJS, Grochla D, Hamann S, Pfetzing-Micklich J, Ludwig A (2012) Thickness-dependence of the B2–B19 martensitic transformation in nanoscale shape memory alloy thin films: zero-hysteresis in 75 nm thick $Ti_{51}Ni_{38}Cu_{11}$ thin films. Acta Mater 60(1):306–313
30. Konig D, Ehmann M, Thienhaus S, Ludwig A (2010) Micro- to nanostructured devices for the characterization of scaling effects in shape-memory thin films. J Microelectromech Syst 19(5):1264–1269
31. Mamivand M, Zaeem MA, Kadiri HE (2015) Effect of variant strain accommodation on the three-dimensional microstructure formation during martensitic transformation: application to zirconia. Acta Mater 87:45–55
32. Simha NK (1997) Twin and habit plane microstructrues due to the tetragonal to monoclinic transformation of zirconia. J Mech Phys Solids 45:261–292
33. Chevalier J, Gremillard L, Virkar AV, Clarke DR (2009) The tetragonal-monoclinic transformation in zirconia: lessons learned and future trends. J Am Ceram Soc 92(9):1901–1920
34. Heuer AH, Ruhle M, Marshall DB (1990) On the thermoelastic martensitic transformation in tetragonal zirconia. J Am Ceram Soc 73(4):1084–1093
35. Jin XJ (2005) Martensitic transformation in zirconia containing ceramics and its applications. Curr Opin Solid State Mater Sci 9(6):313–318
36. Zeng XM, Du Z, Schuh CA, Tamura N, Gan CL (2016) Microstructure, crystallization and shape memory behavior of titania and yttria co-doped zirconia. J Eur Ceram Soc 36(5):1277–1283
37. Swain MV (1986) Shape memory behaviour in partially stabilized zirconia ceramics. Nature 322:234–236
38. Zhang Y, Jin X, Hsu TY, Zhang Y, Shi J (2002) Shape-memory effect in Ce-Y-TZP ceramics. Mater Sci Forum 394–395:573–576
39. Zeng X, Du Z, Schuh CA, Gan CL (2017) Enhanced shape memory and superelasticity in small-volume ceramics: a perspective on the controlling factors. MRC Commun 7(4):747–754
40. Du Z, Ye P, Zeng XM et al (2017) Synthesis of monodisperse CeO_2 -ZrO_2 particles exhibiting cyclic superelasticity over hundreds of cycles. J Am Ceram Soc 100(9):4199–4208
41. Yu HZ, Hassani-Gangaraj M, Du Z, Gan CL, Schuh CA (2017) Granular shape memory ceramic packings. Acta Mater 132:455–466
42. Zhao X, Lar A, Schuh CA (2017) Shape memory zirconia foams through ice templating. Scr Mater 135:50–53
43. Du Z, Zeng XM, Liu Q, Lai A, Amini S, Miserez A, Schuh CA, Gan CL (2015) Size effects and shape memory properties in ZrO_2 ceramic micro- and nano-pillars. Scr Mater 101:40–43
44. Zeng XM, Lai A, Gan CL, Schuh CA (2016) Crystal orientation dependence of the stress-induced martensitic transformation in zirconia-based shape memory ceramics. Acta Mater 116:124–135
45. Du Z, Zhou X, Ye P, Zeng X, Gan CL (2020) Shape-memory actuation in aligned zirconia nanofibers for artificial muscle applications at elevated temperatures. ACS Appl Nano Mater 3:2156–2166
46. Crystal IR, Lai A, Schuh CA (2020) Cyclic martensitic transformations and damage evolution in shape memory zirconia: single crystals vs polycrystals. J Am Ceram Soc 103:4678–4690
47. Kimura T, Newnham RE, Cross LE (1981) Shape-memory effect in PLZT ferroelectric ceramics. Phase Trans 2(2):113–130
48. Li JY, Rogan RC, Ustündag E, Bhattacharya K (2005) Domain switching in polycrystalline ferroelectric ceramics. Nat Mater 4(10):776–781
49. Ren X, Zhang LX (2006) Electro-shape-memory effect in ferroelectric martensite. Mater Sci Eng A 438–440:1071–1076
50. Ren X (2004) Large electric-field-induced strain in ferroelectric crystals by point-defect-mediated reversible domain switching. Nat Mater 3(2):91–94
51. Setter N, Damjanovic D, Eng L, Fox G, Gevorgian S, Hong S, Kingon A, Kohlstedt H, Park NY, Stephenson GB, Stolitchnov I, Taganstev AK, Taylor DV, Yamada T, Streiffer S (2006) Ferroelectric thin films: review of materials, properties, and applications. J Appl Phys 100(5):51606
52. Wadhawan VK, Kernion MC, Kimura T, Newnham RE (1981) The shape-memory effect in PLZT ceramics. Ferroelectrics 37(1):575–578
53. Yan Y, Feng Y (2016) Large and stable shape memory effect realized by defect dipoles in acceptor-doped ferroelectric ceramics. J Am Ceram Soc 99(1):206–210

54. Yang P, Payne DA (1992) Thermal stability of field-forced and field-assisted antiferroelectric-ferroelectric phase transformations in Pb(Zr, Sn, Ti)O_3. J Appl Phys 71(3):1361–1367
55. Zhuo F, Li Q, Zhou Y, Ji Y, Yan Q, Zhang Y, Xi X, Chu X, Cao W (2018) Large field-induced strain, giant strain memory effect, and high thermal stability energy storage in (Pb, La)(Zr, Sn, Ti)O_3 antiferroelectric single crystal. Acta Mater 148:28–37
56. Wang L, Zhou Z, Zhao X, Liu Z, Liang R, Dong X (2017) Enhanced strain effect of aged acceptor-doped $BaTiO_3$ ceramics with clamping domain structures. Appl Phys Lett 110(10):102904
57. Liu W, Zhang L, Chen W, Li S, Ren X (2011) Large digital-characterized electrostrain in Mn-doped (Pb, Sr)TiO_3 electro-shape-memory ceramics. Appl Phys Lett 99(9):92907
58. Rojac T, Kosec M, Damjanovic D (2011) Large electric-field induced strain in $BiFeO_3$ ceramics. J Am Ceram Soc 94(12):4108–4111
59. Du G, Liang R, Wang L, Li K, Zhang W, Wang G, Dong X (2013) Large stable strain memory effect in poled Mn-doped $Pb(Mn_{1/3}Sb_{2/3})O_3$-Pb(Zr, Ti)O_3 ceramics. Appl Phys Lett 102(16):162907
60. Liu W, Chen W, Yang L, Wang Y, Zhang L, Zhou C, Li S, Ren X (2006) Electro-shape-memory effect in hybrid doped $BaTiO_3$ ceramics. Mater Sci Eng A 438–440:350–353
61. Silva J, Reyes A, Esparza H, Camocho H, Fuentes L et al (2011) $BiFeO_3$: a review on synthesis, doping and crystal structure. Integr Ferroelectr 126(1):47–59
62. Čebela M, Zagorac D, Batalović K, Radaković J, Stojadinović B, Spasojević V, Hercigonja R (2017) $BiFeO_3$ perovskites: a multidisciplinary approach to multiferroics. Ceram Int 43(1):1256–1264
63. Zeches RJ, Rossell MD, Zhang JX, Hatt AJ, He Q, Yang C-H, Kumar A, Wang CH, Melville A, Adamo C, Sheng G, Chu YH, Ihlefeld JF, Erni R, Ederer C, Gopalan V, Chen LQ, Schlom DG, Spaldin NA, Martin LW, Ramesh R (2009) A strain-driven morphotropic phase boundary in $BiFeO_3$. Science 326(5955):977–980
64. Ahart M, Somayazulu M, Cohen RE, Ganesh P, Dera P, Mao HK, Hemley RJ, Ren Y, Liermann P, Wu Z (2008) Origin of morphotropic phase boundaries in ferroelectrics. Nature 451(7178):545–548
65. Lummen TTA, Gu Y, Wang J, Lei S, Xue F, Kumar A, Barnes AT, Barnes E, Denev S, Belianinov A, Holt M, Morozovska AN, Kalinin S, Chen LQ, Gopalan V (2014) Thermotropic phase boundaries in classic ferroelectrics. Nat Commun 5:3172
66. Wang Y (2009) Field-induced inter-ferroelectric phase transformations and domain mechanisms in high-strain piezoelectric materials: insights from phase field modeling and simulation. J Mater Sci 44(19):5225–5234
67. Cross LE (1995) Boundary conditions for shape memory in ceramic materials systems. J Intell Mater Syst Struct 6:55–61
68. Zhang JX, Xiang B, He Q, Seidel J, Zeches RJ, Yu P, Yang SY, Wang CH, Chu YH, Martin LW, Minor AM, Ramesh R (2011) Large field-induced strains in a lead-free piezoelectric material. Nat Nanotechnol 6(2):98–102
69. Eyert V (2002) The metal-insulator transitions of VO_2: a band theoretical approach. Ann Phys 11:650–702
70. Rúa A, Fernández FE, Sepúlveda N (2010) Bending in VO_2-coated microcantilevers suitable for thermally activated actuators. J Appl Phys 107(7):74506
71. Jones AC, Berweger S, Wei J, Cobden D, Raschke MB (2010) Nano-optical investigations of the metal-insulator phase behavior of individual VO_2 microcrystals. Nano Lett 10(5):1574–1581
72. Cao J, Gu Y, Fan W, Chen LQ, Ogletree DF, Chen K, Tamura N, Kunz M, Barrett C, Seidel J, Wu J (2010) Extended mapping and exploration of the vanadium dioxide stress-temperature phase diagram. Nano Lett 10(7):2667–2673
73. Kosuge K, Kachi S (1976) Phase diagram of $Fe_xV_{1-x}O_2$ in the $0 \leq x \leq 0.25$ region. Mat Res Bull 11:255–262
74. Marezio M, McWhan DB, Remeika JP, Dernier PD (1972) Structural aspects of the metal-insulator transitions in Cr-doped VO_2. Phys Rev B 5:2541
75. Ghedira M, Vincent H, Marezio M (1977) Structural aspects of the metal-insulator $V_{0.985}AI_{0.015}O_2$. Phys Rev B 22:423–438
76. Cao J, Fan W, Zhou Q, Sheu E, Liu A, Barrett WuJ (2010) Colossal thermal-mechanical actuation via phase transition in single-crystal VO_2 microcantilevers. J Appl Phys 108(8):83538
77. Rúa A, Cabrera R, Coy H, Merced E, Sepúlveda N, Fernández FE (2012) Phase transition behavior in microcantilevers coated with M1-phase VO_2 and M2-phase VO_2: Cr thin films. J Appl Phys 111(10):104502
78. Cabrera R, Merced E, Sepúlveda N (2014) Performance of electro-thermally driven VO_2-based MEMS actuators. J Microelectromech Syst 23(1):243–251
79. Cabrera R, Merced E, Sepúlveda N (2013) A micro-electro-mechanical memory based on the structural phase transition of VO_2. Phys Status Solidi A 210(9):1704–1711
80. Liu K, Cheng C, Cheng Z, Wang K, Ramesh R, Wu J (2012) Giant-amplitude, high-work density microactuators with phase transition activated nanolayer bimorphs. Nano Lett 12(12):6302–6308
81. Du J, Gao Y, Luo H, Kang L, Zhang Z, Chen Z, Cao C (2011) Significant changes in phase-transition hysteresis for Ti-doped VO_2 films prepared by polymer-assisted deposition. Sol Energy Mater Sol Cells 95(2):469–475
82. Romanyuk A, Steiner R, Marot L, Oelhafen P (2007) Temperature-induced metal–semiconductor transition in W-doped VO_2 films studied by photoelectron spectroscopy. S Sol Energy Mater Sol Cells 91(19):1831–1835
83. Jin P, Tanemura S (1996) $V_{1-x}Mo_xO_2$ thermochromic films deposited by reactive magnetron sputtering. Thin Solid Films 281–282:239–242
84. Wang X, Rogalla D, Ludwig A (2018) Influences of W content on the phase transformation properties and the associated stress change in thin film substrate combinations studied by fabrication and characterization of thin film $V_{1-x}W_xO_2$ materials libraries. ACS Comb Sci 20(4):229–236
85. Wang X, Suhr E, Banko L, Salomon S, Ludwig A (2020) Influences of Cr content on the phase transformation properties and stress change in V–Cr–O thin-film libraries. ACS Appl Electron Mater 2:1176–1183
86. Huber JE, Fleck NA, Ashby MF (1997) The selection of mechanical actuators based on performance indices. Proc R Soc Lond A 453:2185–2205